energies

MDPI

Article

Effects of Reservoir Heterogeneity on CO_2 Dissolution Efficiency in Randomly Multilayered Formations

Xiaoyu Fang [1], Yanxin Lv [1,2,3,*], Chao Yuan [4], Xiaohua Zhu [5], Junyang Guo [1], Weiji Liu [5] and Haibo Li [3]

1 Southern Marine Science and Engineering Guangdong Laboratory (Zhanjiang), Zhanjiang 524006, China; fangxy@zjblab.com (X.F.)
2 Department of Petroleum Geology & Geology, School of Geosciences, University of Aberdeen, Aberdeen AB24 3UE, UK
3 State Key Laboratory of Geomechanics and Geotechnical Engineering, Institute of Rock and Soil Mechanics, Chinese Academy of Sciences, Wuhan 430071, China; hbli@whrsm.ac.cn
4 Shenzhen Key Laboratory of Deep Engineering Sciences and Green Energy, College of Civil and Transportation Engineering, Shenzhen University, Shenzhen 518060, China; 2250471015@email.szu.edu.cn
5 School of Mechatronic Engineering, Southwest Petroleum University, Chengdu 610500, China
* Correspondence: lv.yanxin@hotmail.com

Abstract: Carbon dioxide (CO_2) dissolution is the secondary trapping mechanism enhancing the long-term security of CO_2 in confined geological formations. CO_2 injected into a randomly multilayered formation will preferentially migrate along high permeability layers, increasing CO_2 dissolution efficiency. In this study, sequential Gaussian simulation is adopted to construct the stratified saline formations, and two-phase flow based on MRST is established to illustrate the spatial mobility and distribution of CO_2 migration. The results show that gravity index G and permeability heterogeneity σ_Y^2 are the two predominant factors controlling the spatial mobility and distribution of CO_2 transports. The CO_2 migration shows a totally different spatial mobility under different gravity index and heterogeneity. When the permeability discrepancy is relatively larger, CO_2 preferentially migrates along the horizontal layer without accompanying the vertical migration. For the formation controlled by gravity index, CO_2 migration is governed by supercritical gaseous characteristics. For the medium gravity index, the upward and lateral flow characteristics of the CO_2 plume is determined by gravity index and heterogeneity. When the gravity index is smaller, permeability heterogeneity is the key factor influencing CO_2 plume characteristics. Permeability heterogeneity is the decisive factor in determining final CO_2 dissolution efficiency. This investigation of CO_2 mobility in randomly multilayered reservoirs provides an effective reference for CO_2 storage.

Keywords: geological CO_2 storage; heterogeneity; dissolution efficiency; upscaling permeability; CO_2 plume

check for updates

Citation: Fang, X.; Lv, Y.; Yuan, C.; Zhu, X.; Guo, J.; Liu, W.; Li, H. Effects of Reservoir Heterogeneity on CO_2 Dissolution Efficiency in Randomly Multilayered Formations. *Energies* **2023**, *16*, 5219. https://doi.org/10.3390/en16135219

Academic Editor: Rouhi Farajzadeh

Received: 25 May 2023
Revised: 27 June 2023
Accepted: 29 June 2023
Published: 7 July 2023

1. Introduction

Global warming is the greatest existential challenge facing humanity according to the Intergovernmental Panel on Climate Change (IPCC) Report [1]. Global warming may threaten human life security and social sustainable development [2]. Geological carbon sequestration is an effective measure against global climate change since it can mitigate climate impacts and reduce greenhouse gas emission [3,4]. Saline aquifers in deep geological formations are predominantly candidates for geological CO_2 sequestration given their hydrodynamic, geological, and thermal conditions [5,6]. It is estimated that geological reservoirs have a potential storage capacity between 8000 and 55,000 Gt of CO_2, representing a sufficient capacity to store over 200 years of current carbon dioxide emissions [7,8].

CO_2 is in supercritical state when injected into saline aquifers (the pressure and temperature of supercritical CO_2 are 7.382 MPa and 31.048 °C, respectively) [9]. CO_2

trapping mechanisms are mainly as follows: stratigraphic or structural, solubility, residual, and mineral trapping [10–14]. For structural trapping, supercritical carbon dioxide is confined as a buoyant immiscible phase within the reservoir, restrained by the structure and the seal rock. Due to residual pressure or capillary pressure, the immobilization of CO_2 occupies the small pores of the saline aquifer during CO_2 injection [15–17]. The fluid–rock interaction of the aquifers results in solubility trapping, reducing the amount of mobile CO_2 lying below the cap rock and ensuring the long-term security of CO_2 storage [18]. Furthermore, mineral trapping is considered to be the result of rock-fluid-CO_2 interaction, involving the geochemistry reactions of reservoir minerals such as calcite, dolomite, siderite, etc. Mineral trapping is the slowest but the most permanent and most safe process [19–22].

For CO_2 dissolution trapping mechanisms, CO_2 dissolution efficiency due to rock-fluid-CO_2 interaction is controlled by reservoir heterogeneity on all scales [23,24]. Many previous studies have extensively investigated the effect of the geological heterogeneity on CO_2 trapping by experiment, field data and numeral simulation. Kim et al. [25] carried out Darcy-scale multiphase flow experiments on a heterogeneous specimen to obtain CO_2 saturation during both drainage and imbibition. Sohal et al. [26] studied the effect of heterogeneous wettability distribution on CO_2 storage efficiency, which showed that both heterogeneously distributed wettability and higher temperature accelerated the vertical CO_2 migration significantly and reduced storage capacity. Singh et al. [27] investigated CO_2 dissolution and local capillary trapping in permeability and capillary heterogeneous reservoir, which suggested that vertical distance between the centers of mass of the supercritical CO_2 and dissolved CO_2 plumes is larger for heterogeneous reservoirs. Onoja et al. [28] investigated the relevance of representing relative permeability variations in the sealing formation, the results demonstrate that gradational changes at the base of the caprock could influence the pressure changes propagating vertically into the caprock from the saline aquifer. Mouche et al. [29] presented an upscaled model for the vertical migration of the CO_2 plume, the results illustrate that the upscaled saturation is controlled by the capillary pressure at the interface of the connected layers. Green et al. [30] studied the heterogeneity effect of vertical permeability on CO_2 long-term migration and showed that the heterogeneous formation with equivalent effective vertical permeability has a shorter breakthrough time in saline aquifer. Deng et al. [31] investigated the effect of multi-scale heterogeneity on storage capacity, designs of injection wells, injection rate, CO_2 plume migration, and CO_2 potential leakage. Kim et al. [32] and Paiman et al. [33] investigated the fracture heterogeneity, and revealed that fractures can significantly affect the predicted amount of trapped CO_2. Galkin et al. [34] adopted X-ray tomography and electron microscopy for description of rock pore space considering reservoir heterogeneity, considered to be an important method to introduce new methods for the development of complex reservoirs. Martyushev et al. [35–38] modified the geological and hydrodynamic model considering both horizontal and vertical permeability heterogeneities (anisotropy parameter), significantly improving the adaptation of both injection and production wells. Oh et al. [39] researched the injection-induced pressure and buoyancy force in a horizontally and vertically stratified core utilizing a core-flooding system with a 2-D X-ray scanner, concluding that CO_2 movement was primarily controlled by media heterogeneity. Rasmusson et al. [40] constructed strata alternating high and low permeability to investigate CO_2 migration, considering the coupled wellbore-reservoir flow. Although several studies have investigated the effect of heterogeneity on CO_2 migration, there are very limited researches regarding qualitative analysis of CO_2 dissolution efficiency considering small-scale variability in stratification permeability during GCS.

The main objective of this investigation aims to reveal the effect of permeability heterogeneity on CO_2 dissolution efficiency in reservoir-caprock system. The two-phase flow model is implemented in MRST (Matlab Reservoir Simulation Toolbox) [41], a finite-volume based method. It is very convenient to develop new features within MRST. The two-phase flow involves the dissolution of CO_2 into brine and evaporation of H_2O into the CO_2 gaseous state. Mathematical description and model implementation of the simulation model are illustrated in Sections 2 and 3, respectively. Model validation and sensitive analysis of the CO_2 dissolution efficiency are depicted in Section 4. Finally, the conclusions are summarized in Section 5.

2. Mathematical Model

2.1. Extended Reaction System

There are three chemical components (CO_2, H_2O, NaCl) in the geological system. The chemical species is determined by the following equilibrium chemical reactions [42,43]:

$$H_2O(l) \Leftrightarrow H_2O(g),\ K^H = f_g^H / a_l^H \tag{1}$$

$$CO_2(aq) \Leftrightarrow CO_2(g),\ K^C = f_g^C / a_l^C \tag{2}$$

where K^H and K^C are the equilibrium constants for H_2O and CO_2, respectively; f_g^α and a_l^α represent the fugacity and activity of the α component in gas or liquid state.

The equilibrium constants of CO_2 and H_2O relation equations are expressed as:

$$K^\beta = K^{\beta 0} exp \frac{(p_l - p_0)V_\beta}{RT_c} \tag{3}$$

with

$$K^{\beta 0} = 10^{a_\beta + b_\beta T_c + c_\beta T_c^2 + d_\beta T_c^3} \tag{4}$$

where $R = 8.314$ [J·K^{-1}·mol^{-1}] is a universal gas constant; T_c is the temperature in °C; V_β is the mean molar volume of the pure condensed species when pressure changes from p_0 to p_l; a_β, b_β, c_β and d_β are the equation parameters.

When the chemical reaction is at equilibrium, the mole fractions of H_2O in gas x_g^H and CO_2 in liquid x_l^C are illustrated in Equations (3) and (4).

$$x_g^H = \frac{K^H a_l^H}{F^H P_{tot}} \tag{5}$$

$$x_l^C = \frac{F^C \left(1 - x_g^H\right) P_{tot}}{55.508 r'_{co_2} K^C} \tag{6}$$

where F^H and F^C the fugacity coefficients of H_2O and CO_2 in CO_2-rich phase; P_{tot} is the total pressure; r'_{co_2} is the activity coefficient that illustrates the relation between the solubility of aqueous CO_2 in pure water and brine.

The mutual solubilities can be expressed in the following formula:

$$x_g^H = \frac{1 - B - x_l^S}{\frac{1}{A} - B} \tag{7}$$

$$x_l^C = B\left(1 - x_g^H\right) \tag{8}$$

$$A = \frac{K^H}{F^H P_{tot}} \tag{9}$$

$$B = \frac{F^C P_{tot}}{55.508 r'_{co_2} K^C} \tag{10}$$

Mass fractions of H_2O in gas phase (X_g^H) and aqueous CO_2 in liquid brine phase (X_l^C) can be obtained in a concise formula [44]:

$$X_g^H = \frac{18.015 x_g^H}{18.015 x_g^H + 44.01\left(1 - x_g^H\right)} \tag{11}$$

$$X_l^C = \frac{44.01x_l^C}{18.015\left(1 - x_l^C\right)\left(1 + 0.05844m_l^S\right) + 44.01x_l^C} \tag{12}$$

where m_l^S denotes the molality of NaCl in liquid state.

2.2. Mass Transport Equations

Based on the mass balances of the H and C components in the geological system, the component transport equations are given as:

$$\sum_{\alpha=l,g}\left[\frac{\partial\left(\varphi S_\alpha \rho_\alpha X_\alpha^H\right)}{\partial t} + \nabla\cdot\left(X_\alpha^H \rho_\alpha q_\alpha\right) - \nabla\cdot\left(\varphi S_\alpha \rho_\alpha D_\alpha \nabla X_\alpha^H\right)\right] - Q_g^H = 0 \tag{13}$$

$$\sum_{\alpha=l,g}\left[\frac{\partial\left(\varphi S_\alpha \rho_\alpha X_\alpha^C\right)}{\partial t} + \nabla\cdot\left(X_\alpha^C \rho_\alpha q_\alpha\right) - \nabla\cdot\left(\varphi S_\alpha \rho_\alpha D_\alpha \nabla X_\alpha^C\right)\right] - Q_g^C = 0 \tag{14}$$

where $\alpha = l$ and $\alpha = g$ represent the liquid brine and gaseous CO_2-rich phase; φ is the reservoir porosity; S_α is the saturation of the α-phase; ρ_α is the density of the α-phase (kg/m^3); X_α^H and X_α^C indicate the mass fraction of H and C components in the α-phase; D_α is the dispersion tensor ($m^2 \cdot s^{-1}$); Q_g^H and Q_g^C are the source term ($kg \cdot s^{-1}$); q_α is the fluid flux of the α-phase associated with Darcy's velocity:

$$q_\alpha = -\frac{\kappa k_{r\alpha}}{\mu_\alpha}\left(\nabla p_\alpha - \rho_g g \nabla z\right) \tag{15}$$

where κ is the intrinsic permeability (m^2); $k_{r\alpha}$ is the relative permeability of the α-phase; μ_α is the viscosity (pa·s); p_α is the fluid pressure (pa); g is the gravitational acceleration ($m \cdot s^{-2}$); ∇z is the vertical distance (m).

2.3. Constitutive Equation

To set up the multiphase flow simulation, we need the capillary-saturation relationship $P_c(S_w)$. Flooding experiments on core samples from the reservoir are used to develop the empirical relationship between P_c and S_w. Leverett J-function is adopted to normalize the measured data [45–48]:

$$J(S_w) = \frac{p_c}{\sigma \cos\theta}\sqrt{\frac{K}{\varphi}} \tag{16}$$

where σ is the surface tension measured in the laboratory; θ is the contact angle; $\sqrt{K/\varphi}$ is scaling factor proportional to the radius of pore-throat.

Van Genuchten model for the retention curve is used to express the effective liquid saturation of the brine system [49]:

$$S_{l(p_c)} = \begin{cases} 1, & p_c < 0 \\ \left[1 + \left(\sqrt{\frac{k\overline{\varphi}}{k_g \varphi}}\alpha_p p_c\right)^{n_p}\right]^{-m_p}, & p_c \geq 0 \end{cases} \tag{17}$$

where S_l is the effective saturation; $\overline{\varphi}$ and k_g are the mean porosity and mean permeability of the reservoir, respectively; α_p is the scaling parameter for the retention curve.

The relative permeabilities for the liquid and gas phases can be expressed as follows:

$$k_{rl} = k_{rlm}\cdot(S_l)^{\epsilon_p}\left[1 - \left(1 - S_l^{1/m_p}\right)^{m_p}\right]^2 \tag{18}$$

$$k_{rg} = k_{rgm}\cdot(1 - S_l)^{\gamma_p}\left(1 - S_l^{1/m_p}\right)^{2m_p} \tag{19}$$

where k_{rlm}, k_{rgm}, ϵ_p and γ_p are the scaling parameters, the values of the main parameters are as shown in Table 1.

Table 1. Values of the main parameters for relative permeability.

Parameter	Value	Parameter	Value
k_{rlm}	1.0	k_{rgm}	1.0
α_p	5.0	m_p	0.4
ϵ_p	0.5	γ_p	0.5

3. Numerical Implementation

Newton-Raphson Iteration

Liquid pressure (p_l), gas pressure (p_g) and bottom hole pressure (p_{bh}) are chosen as the independent variables during the numerical implementation. Newton-Raphson iteration method is adopted to solve the governing equations. The system of three equations is expressed in compact form:

$$F(x) = 0 \tag{20}$$

where

$$[F] = \begin{bmatrix} F_H \\ F_C \\ F_W \end{bmatrix}, \ [x] = \begin{bmatrix} p_l \\ p_g \\ p_{bh} \end{bmatrix} \tag{21}$$

where F_H, F_C and F_W represent the equilibrium control equations for H_2O, CO_2 and injection wells.

The Newton-Raphson iteration of x is expressed as:

$$J_t^{i+1,k}[\delta x]^{i+1,k} = -[F]_t^{i+1,k} \tag{22}$$

where the Jacobian matrix is:

$$J_t^{i+1,k} = \begin{bmatrix} \frac{\partial F_H}{\partial p_l} & \frac{\partial F_H}{\partial p_g} & \frac{\partial F_H}{\partial p_{bh}} \\ \frac{\partial F_C}{\partial p_l} & \frac{\partial F_C}{\partial p_g} & \frac{\partial F_C}{\partial p_{bh}} \\ \frac{\partial F_W}{\partial p_l} & \frac{\partial F_W}{\partial p_g} & \frac{\partial F_W}{\partial p_{bh}} \end{bmatrix}^{i+1,k} \tag{23}$$

Taylor series is used to update the independent variables:

$$[x]^{i+1,k+1} = [x]^{i+1,k} + [\delta x]^{i+1,k} \tag{24}$$

4. Numerical Simulation

4.1. Model Validation

In order to validate the accuracy of the numerical method, the sharp interface is achieved by moving all of the gaseous CO_2 above the liquid brine, and the plume depth of the interface is given:

$$z(r) = \int_0^h S_g(r,z)dz \tag{25}$$

Figures 1 and 2 show saturation distribution of the gas phase and the comparison of the numerical result with the similarity solution of CO_2 injection in homogenous formation by Nordbotten. Nordbotten et al. [50] derived the similarity solution of carbon dioxide injected into confined aquifers, assuming that a clear interface separates the gaseous CO_2 and brine liquid, as illustrated in Figure 2.

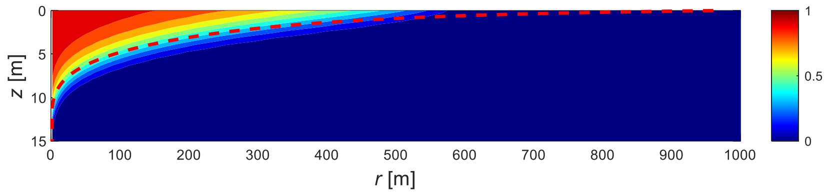

Figure 1. Saturation distribution of the gas phase (the red dotted line is the sharp interface calculated by Equation (25) using our method).

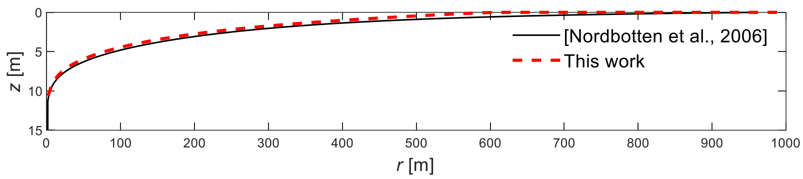

Figure 2. Comparison of the numeral result with the solution by Nordbotten [50].

4.2. Effect of Pressure

The problem of interest here is the injection of supercritical CO_2 through a fully penetrating vertical well beneath the caprock in the deep confined saline aquifer. Sequential Gaussian simulation (SGSIM) as a stochastic method has been developed to generate a series of models of possible reservoir rock heterogeneities [51]. This simulation technique produces equiprobable models of a continuous variable with the appropriate probability distribution and a spatial correlation function. The simplicity and flexibility of the SGSIM code make it particularly appropriate for simulating petrophysical properties such as permeabilities and porosities of the reservoir. The multilayered reservoir is composed of horizontally stratified layers with the sequential Gaussian simulation method by SGSIM code. The permeability is represented by the spatial variability of the intrinsic permeability, and the permeability is rescaled to obtain the reservoir statical property as follows:

$$Y(x) = \overline{Y} + \sigma_Y Y_{std}(x) \tag{26}$$

where $\overline{Y}$ is the intrinsic permeability of the reservoir; σ_Y is the sqrt of variance σ_Y^2, indicating the heterogeneity coefficient of saline aquifers; and $Y_{std}(x)$ is the standardized Gaussian random field with a zero mean and unit variance.

There are two immiscible fluid phases, namely the water-rich brine phase and the CO_2-rich gaseous phase. The brine phase is mainly represented by a high-concentration of NaCl in water. The temperature is considered to be constant during CO_2 injection. The simulation system is represented by an axisymmetric model in the cylindrical system (r, φ, z).

The multilayered formation system is initially saturated with the brine in a hydrostatic state, and the top and bottom boundaries are impermeable boundaries. The liquid pressure at the right boundary increases downward with a vertical gradient. Schematic of the simulation setup is shown in Figure 3. Logarithm permeability distributions of the reservoir beneath the caprock with three different variances σ_Y^2 are illustrated in Figure 4. The specified values of logarithm permeability distributions along the reservoir depth are shown in Figure 5. The larger the variance is, the more heterogeneous the multilayered formation is. The parameters listed in adopted for GCS are illustrated in Table 2.

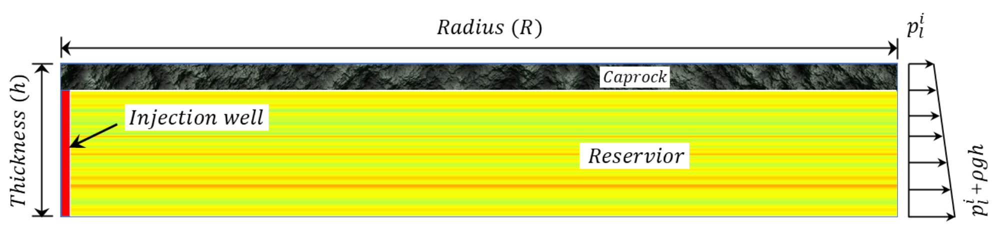

Figure 3. Sketch of the simulation setup (different colors display geological heterogeneities).

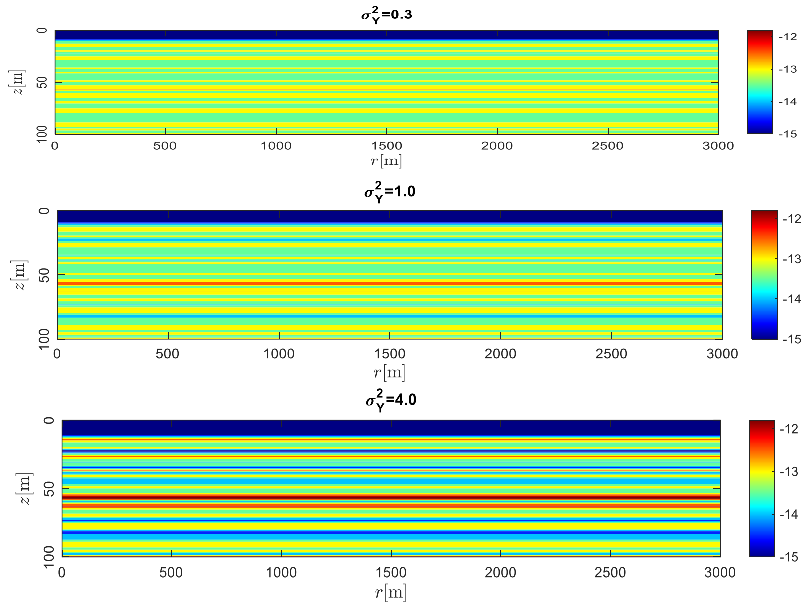

Figure 4. Logarithm permeability distributions of the stratified reservoir with different variances.

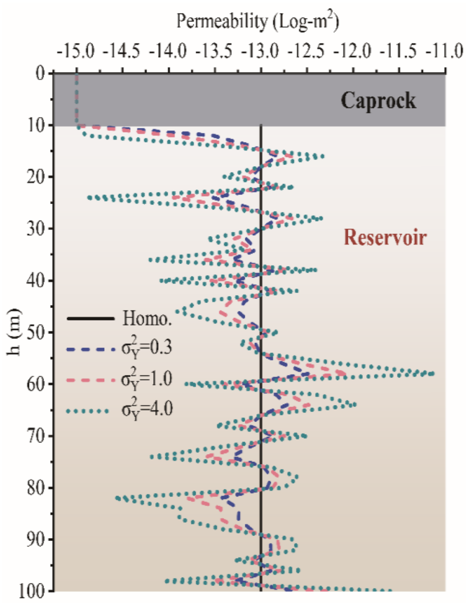

Figure 5. Logarithm permeability distributions along the reservoir depth.

Gravity index G is defined as the ratio of gravity force resulting from vertical permeability, density difference, and reservoir thickness to the viscose force:

$$G = \frac{2\pi(\rho_l - \rho_g)\rho_g g k_h h^2}{Q\mu_l} \tag{27}$$

where ρ_l and ρ_g are the density of the brine liquid and supercritical gaseous phases; k_h is the vertical permeability of the reservoir; h is the vertical thickness of the formation; and Q is the injection rate of the gas phase.

The parameters listed in Table 3 includes different values of injection rate Q, variances σ_Y^2 and gravity index G. Note that gravity index G and variances σ_Y^2 are dimensionless.

Table 2. Summary of the parameters adopted for GCS.

Parameters	Symbol	Units	Values
Domain size	(R, b)	[m]	(3000, 100)
Grid discretization	(Nr, Nz)	[–]	(100, 100)
Porosity	ϕ	[–]	0.1
Mean permeability	k_g	[m^2]	10^{-13}
Initial liquid pressure	p_l	[bar]	150
Initial gas pressure	p_g	[bar]	1
Well radius	r_w	[m]	0.1
Total injection mass	M_{inj}	[Mt]	2.5
Residual saturations	(S_{lr}, S_{gr})	[–]	(0.2, 0)
Hydrodynamic dispersivities	$(\alpha L, \alpha T)$	[m]	(5, 1)
Molecular diffusion coefficient	D_m	[m^2·s^{-1}]	10^{-9}
Salinity	m_l^S	[molal]	0.1
Temperature	T_c	[°C]	60
Simulation time	t	[s]	3.15×10^7

Table 3. Gravity index calculations in different simulated cases.

Case	$Q(Mt/y)$	k_g(m^2)	σ_Y^2	G
1	7.5	10^{-13}	0	0.6
2	2.5	10^{-13}	0	1.8
3	0.8	10^{-13}	0	5.6
4	0.8	10^{-13}	0.3	5.6
5	0.8	10^{-13}	1.0	5.6
6	0.8	10^{-13}	4.0	5.6
7	2.5	10^{-13}	0.3	1.8
8	2.5	10^{-13}	1.0	1.8
9	2.5	10^{-13}	4.0	1.8
10	7.5	10^{-13}	0.3	0.6
11	7.5	10^{-13}	1.0	0.6
12	7.5	10^{-13}	4.0	0.6

4.3. Spatial Mobility and Distribution of CO_2

Effective gas saturation S_{ge} is adopted to interpret the CO_2 plume evolution during CO_2 injection:

$$S_{ge} = \frac{S_g - S_{gr}}{1 - S_{lr} - S_{gr}} \tag{28}$$

where S_{lr} and S_{gr} are the residual liquid and gas saturation, respectively.

Dimensionless time variable t^* is adopted to facilitate the interpretation of CO_2 dissolution efficiency:

$$t^* = \frac{t}{t_c} \tag{29}$$

$$t_c = \frac{\varphi \mu_l h}{(\rho_l - \rho_g) g k_h} \tag{30}$$

where t_c is the characteristic time, an important indicator of the migration time from the bottom of reservoir to the top due to buoyant forces.

Figure 6 shows the spatial mobility and distribution of CO_2 over time. The plots in the first and second column in Figure 6 show the migration path for Cases 10 and 12, respectively. At the initial injection stage, the spatial mobility of CO_2 shows a quite different distribution behave for heterogeneous reservoirs when $t = 0.01t^*$. For the smaller formation heterogeneity such as $\sigma_Y^2 = 0.3$, the upwind and lateral migration of the CO_2 plume is relatively more uniform around the injection well, compared with heterogeneity

$\sigma_Y^2 = 4.0$. The variation difference between the logarithm permeability distributions along the reservoir depth is relatively larger for Case 12, as illustrated in Table 2, and the mainly horizontal flow path is generated as the CO_2 migrates along the horizontal layer with the maximum permeability at time $t = 0.01t^*$. While $t = 0.05t^*$, CO_2 starts the migration along the layers with the relatively high permeabilities in the multilayered formation. Due to the big discrepancies in permeability as shown in Figure 5, there are certain relatively low permeability layers that restricts the upwind migration of CO_2 with heterogeneity $\sigma_Y^2 = 4.0$. It can be observed from the second column in Figure 6 that the CO_2 preferentially migrates along the horizontal layer, without accompanying the vertical migration. While for the first column in Figure 6, the CO_2 migrates along the horizontal layers in the early injection period ($t \leq 0.4t^*$), and CO_2 continue to transport horizontally and gradually migrate upwind to the top of the reservoir due to buoyancy forces in the late injection stage ($t \geq 0.4t^*$). It is indicated that permeability heterogeneity is the primary factor influencing the spatial mobility and distribution of CO_2 injection.

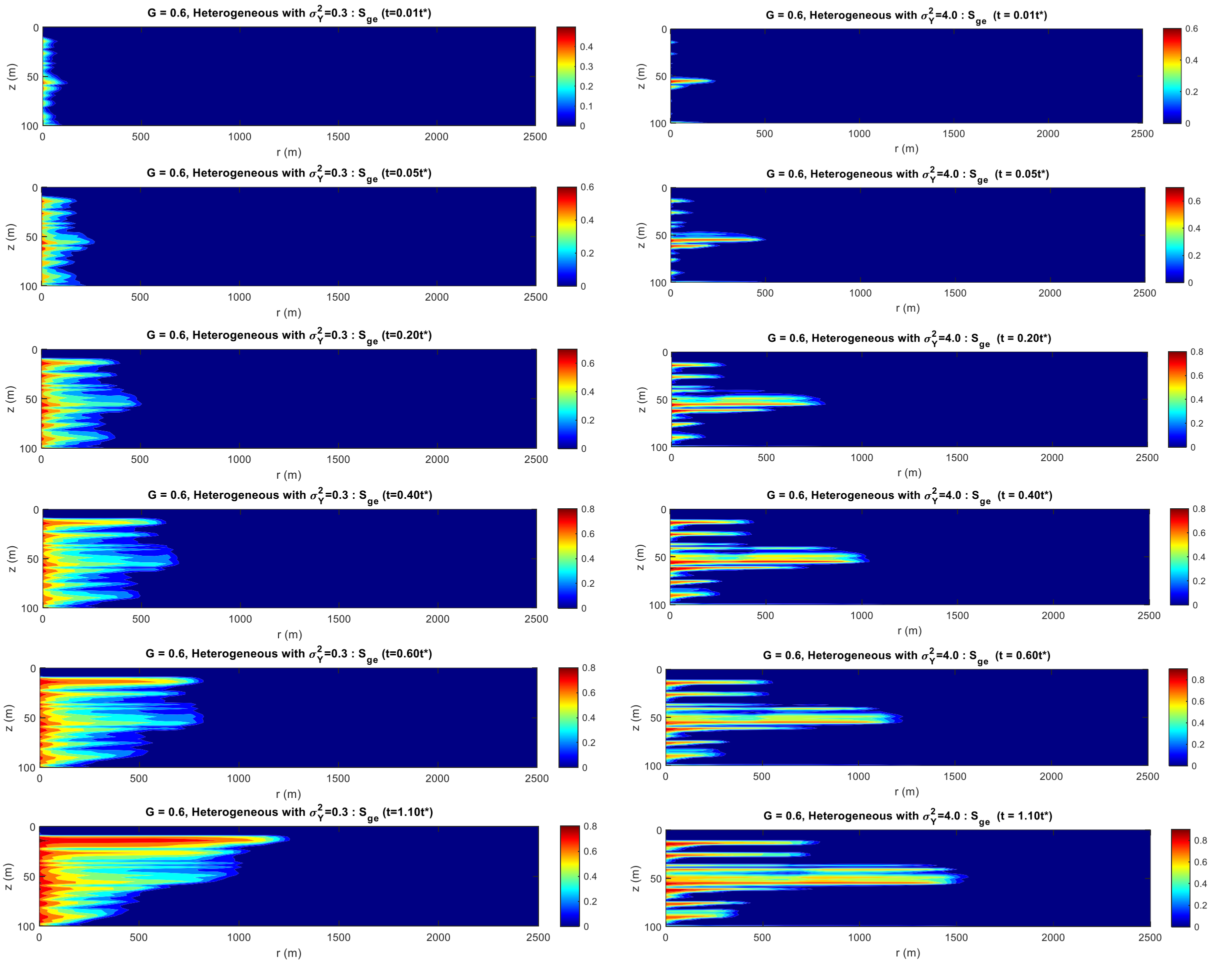

Figure 6. Spatial mobility and distribution of CO_2 for Case 10 and Case 12 over time during CO_2 injection.

4.4. Effect of Heterogeneity and Gravity Index

Figures 7–9 show the spatial distribution of the effective saturation (S_{ge}) and mass fraction of aqueous CO_2 in brine (X_l^C) at the end of the injection ($t = 1.1t^*$). The influences of heterogeneity and gravity index on CO_2 migration are compared for the simulated cases.

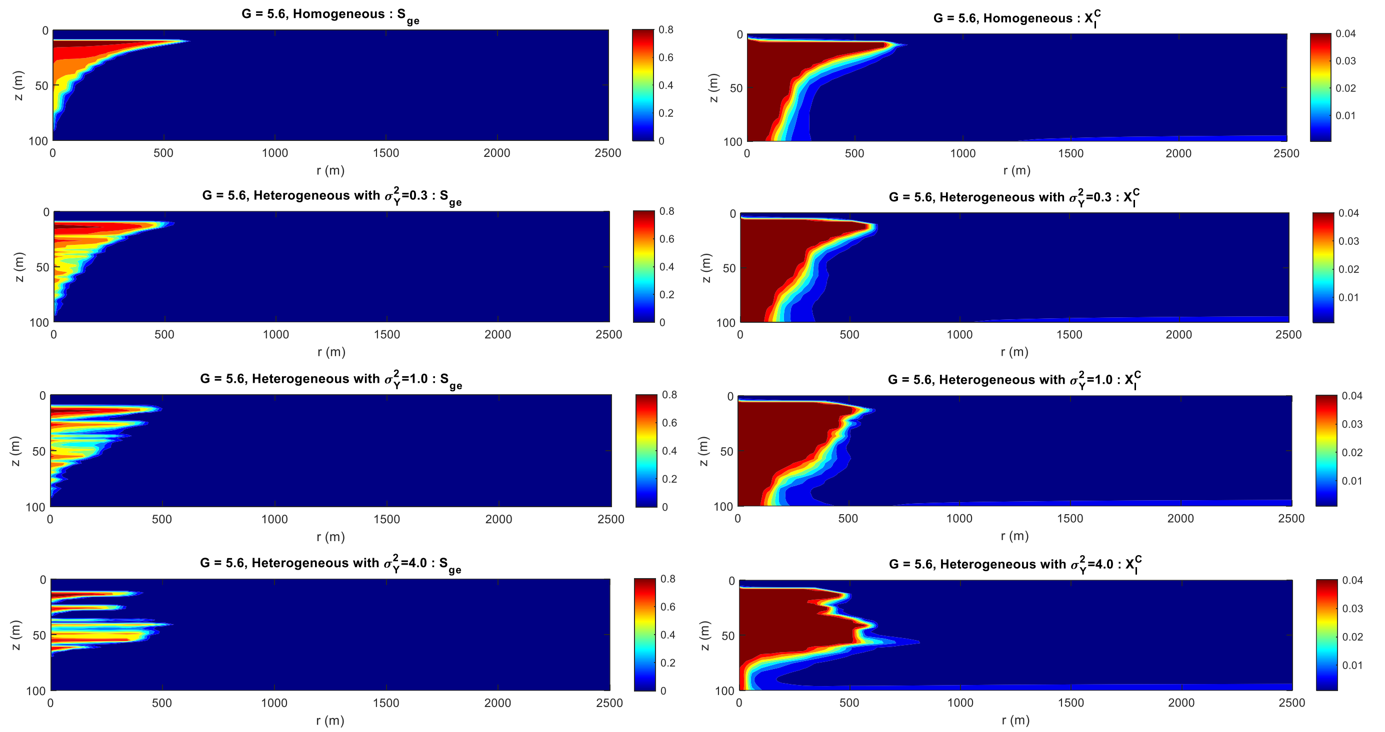

Figure 7. Distribution of the effective saturation (S_{ge}) and mass fraction of aqueous CO_2 in brine (X_l^C) when $t = 1.1t^*$.

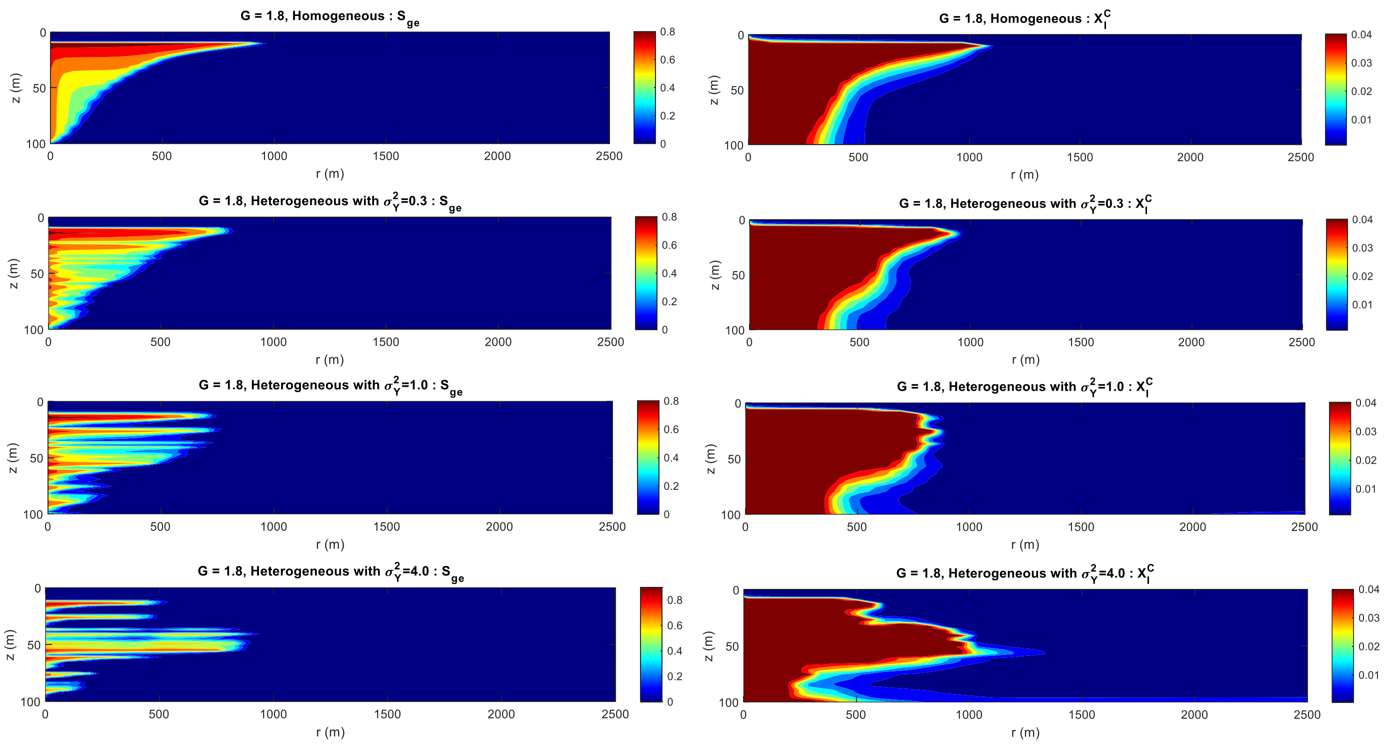

Figure 8. Distribution of the effective saturation (S_{ge}) and mass fraction of aqueous CO_2 in brine (X_l^C) when $t = 1.1t^*$.

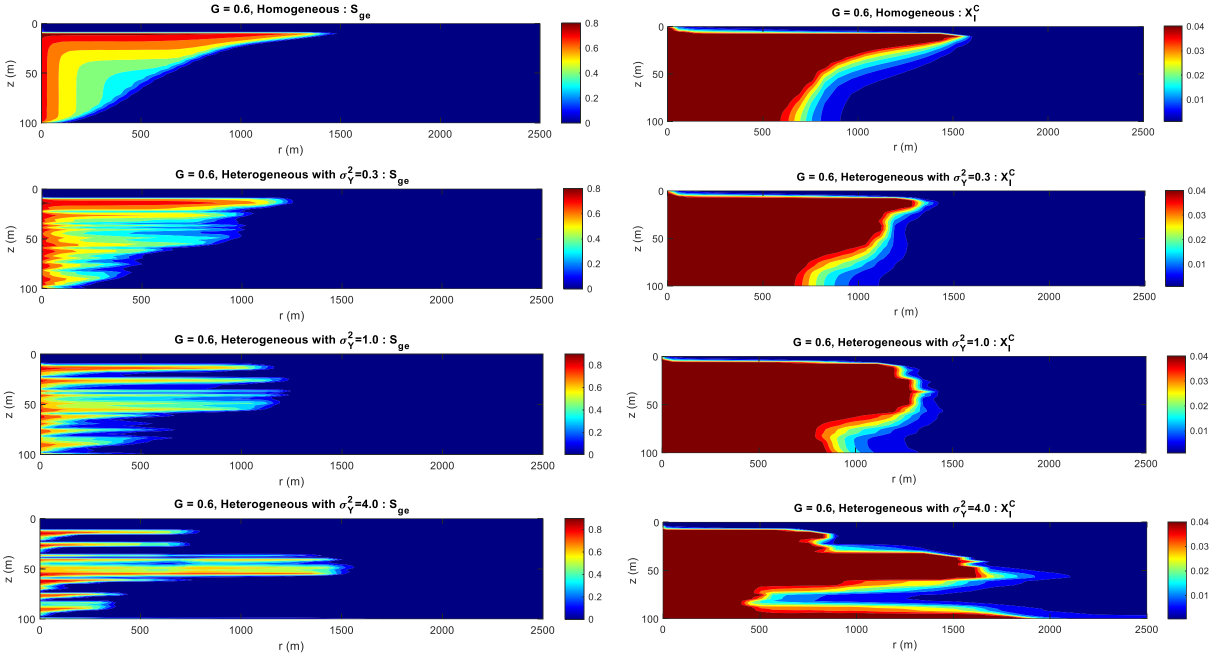

Figure 9. Distribution of the effective saturation (S_{ge}) and mass fraction of aqueous CO_2 in brine (X_l^C) when $t = 1.1t^*$.

For homogenous formation, the low viscosity CO_2 tends to migrate to the top of the geological structure due to the density difference between the CO_2 plume and the brine for Cases 1, 2, and 3. During the upward migration of the CO_2 plume, a large amount of gas phase migrates to the top of the aquifer due to buoyancy forces. The effective saturation at the top of the formation is relatively higher than that of the lower formation. It can be seen from Cases 1, 2, and 3 that mass injection rate or the gravity index has obvious influence on CO_2 plume migration. The higher the CO_2 injection rate, the farther the CO_2 plume migration. The CO_2 migration sketch is approximately proportional to the CO_2 injection rate. The variation of the mass fraction of aqueous CO_2 in brine shows a similar trend.

For the multilayered formation, gravity index and heterogeneity are the two predominant factors controlling CO_2 plume migration. For the bigger gravity index such as $G = 5.6$, gravity index is the dominant factor controlling CO_2 migration, as illustrated in Figure 7. When the formation heterogeneity is relatively small ($\sigma_Y^2 \leq 1$), the distribution and mobility of CO_2 migration are almost identical at the end of the injection. While $\sigma_Y^2 = 4$, there are some low permeability layers that impedes the vertical flow of CO_2 migration. The CO_2 migrates laterally along the preferentially high permeability layers away from the injection wells. The CO_2 migration distance is almost the same for Cases 3, 4, 5, and 6 at a relatively small injection rate. For the medium gravity index such as $G = 1.8$, the influence of heterogeneity is increasing. When $\sigma_Y^2 \geq 1$, the distribution and mobility of CO_2 migration is discontinuous due to the permeability heterogeneity. For smaller heterogeneity such as $\sigma_Y^2 = 0.3$, the effective gas saturation is almost the same as that of the homogenous formation. The gravity index and heterogeneity could influence the upward and lateral migration of the CO_2 plume at the medium injection rate. For the smaller gravity index such as $G = 0.6$, formation heterogeneity is the key factor influencing CO_2 distribution. CO_2 migrates laterally along the high permeability layers, and the corresponding lower permeability layers obstruct the upward migration of the CO_2 plume. The farther the CO_2 migration, the bigger the permeability variance σ_Y^2. It is suggested that with the increase of heterogeneity variance σ_Y^2, horizontal flow paths are generated and the heterogeneity characteristics of effective saturation become more obvious. The existence of high permeability layers in the multilayered formation is conducive to CO_2 storage. The larger the permeability variance σ_Y^2 is at field level, the more CO_2 will be constrained underground during CO_2 storage.

4.5. CO_2 Dissolution Efficiency

Carbon dioxide dissolution efficiency η is the mass quantification of CO_2 dissolved into brine with respect to the CO_2 injected into the formation per unit of time, as shown in:

$$\eta(t) = \frac{M'(t + \Delta t) - M'(t)}{M(t + \Delta t) - M(t)} \tag{31}$$

where $M'(t)$ and $M(t)$ are the mass of the CO_2 dissolved into the brine and the total CO_2 injected into the well at time t, respectively; Δt is the time step. The CO_2 dissolved into the brine is indirectly calculated from the undissolved gaseous state as follows:

$$\eta(t) = \frac{Qt - \sum_i \left[\varphi V_i S_g \rho_g X_g^C\right]^t}{Qt} \tag{32}$$

where Q is the mass injection rate of CO_2; V_i is the volume of the i-th grid cell; and X_g^C is the mass fraction of CO_2 in gaseous state.

Figure 10 shows the temporal evolution of CO_2 dissolution efficiency in brine during $t = 1.1t^*$, and the effects of gravity index and heterogeneity on CO_2 dissolution efficiency are investigated. It can be observed from the first column in Figure 10 that the gravity index has a prominent influence on CO_2 dissolution efficiency. The higher the gravity index, the more CO_2 is dissolved in brine. CO_2 is more likely to dissolve in brines at a lower injection rate. For homogenous formation, the CO_2 dissolution efficiency is lower than that of the heterogeneous stratum at the same gravity index and the permeability heterogeneity is more conducive to CO_2 dissolution. When the gravity index is relatively bigger such as $G = 5.6$, the formation is gravity controlled and the influence of permeability heterogeneity on CO_2 dissolution efficiency is not obvious. For bigger and medium gravity indices ($G \geq 1.8$), the CO_2 dissolution efficiency increases with the increase of heterogeneity coefficient σ_Y^2, and tends to achieve a stable value. As seen from $G = 0.6$ in Figure 10, with the increase of the heterogeneity coefficient σ_Y^2, the curve of CO_2 dissolution efficiency is also gradually increasing at the same time. The second column in Figure 10 shows that the permeability heterogeneity is the decisive factor in determining the finial CO_2 dissolution efficiency. The dissolution curve shows a decreasing trend during CO_2 injection. During the initial injection period, the dissolution curve with the higher gravity index is relatively higher, and then the gaps between these curves become smaller and smaller, approaching a constant value. It should be noted that the CO_2 dissolution efficiency curve with the maximum gravity index ($G = 5.6$) is slightly higher for CO_2 injection processes.

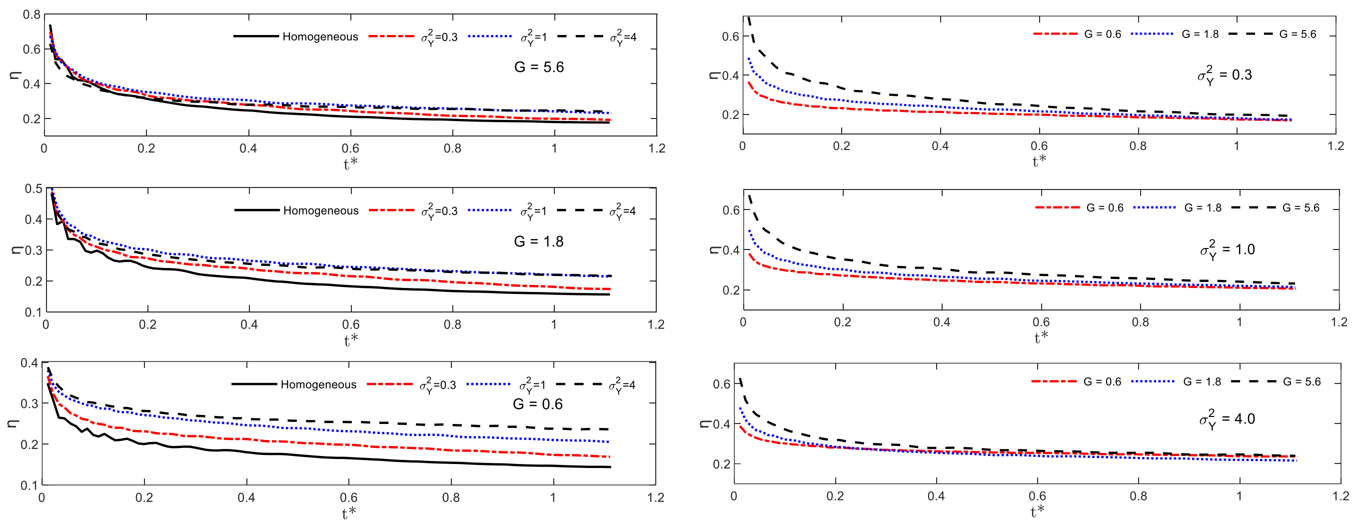

Figure 10. Temporal evolution of CO_2 dissolution efficiency in brine.

5. Conclusions

In this paper, sequential Gaussian simulation is adopted to construct the multilayered saline formations, and two-phase flow based on MRST is developed to investigate the spatial mobility and distribution of CO_2 being injected into the multilayered reservoir. The main conclusions are as follows:

(1) The permeability heterogeneity is the primary factor influencing the spatial mobility and distribution of CO_2 injection. Heterogeneity variances σ_Y^2 is considered to be an ideal representation of reservoir permeability.
(2) For the formation with the smaller heterogeneity, the upwind and lateral migration of the CO_2 plume is relatively more uniform around the injection well. For the bigger heterogeneity, CO_2 preferentially migrates along the horizontal layer without accompanying the vertical migration.
(3) For the formation with the bigger gravity index, gravity index is the dominant factor controlling CO_2 migration. For the medium gravity index, the upward and lateral migration of the CO_2 plume is determined by the gravity index and heterogeneity. For the smaller gravity index, formation heterogeneity is the key factor influencing CO_2 distribution.
(4) The dissolution curve shows a decreasing trend during CO_2 injection. The dissolution curve with the higher gravity index is relatively higher at the initial injection period and the gap difference between dissolution curves approaches to a constant value. The permeability heterogeneity is the decisive factor in determining the finial CO_2 dissolution efficiency.
(5) From a practical point of view, most GCS field sites operate under $G \ll \sigma_Y^2$. It is suggested to store CO_2 in formations with relatively larger heterogeneity coefficient σ_Y^2.
(6) Reactive 3-Phase flow model for geological sequestration is considered for future research. It will be a more sophisticated analysis of the GCS, incorporating the chemical reaction among aqueous species and rock-forming minerals, as well as the partition between gaseous CO_2 phase and liquid brine phase.

Author Contributions: All of the authors contributed to publishing this paper. Y.L. and X.F. contributed to the research goals and aims; J.G., C.Y. and X.Z. contributed to the writing; W.L. and H.L. contributed to the language and pictures. All authors have read and agreed to the published version of the manuscript.

Funding: This work was financially supported by National Natural Science Foundation of China (No. 52274231 and No. 52034006), ZhanJiang Science and Technology Project (No. 2022A01061), and ZhanJiangWan Project (No. ZJW-2022-08-07).

Data Availability Statement: Data will be made available on request.

Acknowledgments: Special thanks to Y.F. Wang, who is a scientist at IFPEN (Rueil-Malmaison, France) and the developer of the two-flow code.

Conflicts of Interest: The authors declare that they have no known competing financial interests or personal relationships that could have appeared to influence the work reported in this paper.

References

1. IPCC. Climate change 2007: Mitigation of climate change: Contribution of working group III to the fourth assessment report of the intergovernmental panel on climate change. *Choice Rev. Online* **2008**. [CrossRef]
2. Haszeldine, R.S.; Flude, S.; Johnson, G.; Scott, V. Negative emissions technologies and carbon capture and storage to achieve the Paris agreement commitments. *Phil. Trans. R. Soc. A* **2018**, *376*, 20160447. [CrossRef] [PubMed]
3. Song, H.; Huang, G.; Li, T.; Zhang, Y.; Lou, Y. Analytical model of CO_2 storage efficiency in saline aquifer with vertical heterogeneity. *J. Nat. Gas Sci. Eng.* **2014**, *18*, 77–89. [CrossRef]
4. Vilarrasa, V.; Bolster, D.; Olivella, S.; Carrera, J. Coupled hydromechanical modeling of CO_2 sequestration in deep saline aquifers. *Int. J. Greenh. Gas Control* **2010**, *4*, 910–919. [CrossRef]
5. Riaz, A.; Hesse, M.; Tchelepi, H.A.; Orr, F.M. Onset of convection in a gravitationally unstable diffusive boundary layer in porous media. *J. Fluid Mech.* **2006**, *548*, 87–111. [CrossRef]

6. Fang, Y.; Baojun, B.; Dazhen, T.; Dunn-Norman, S.; Wronkiewicz, D. Characteristics of CO_2 sequestration in saline aquifers. *Petrol. Sci.* **2010**, *7*, 83–92.
7. Kearns, J.; Teletzke, G.; Palmer, J.; Thomann, H.; Kheshgi, H.; Chen, Y.H.H.; Herzog, H. Developing a consistent database for regional geologic CO_2 storage capacity worldwide. *Energy Procedia* **2017**, *114*, 4697–4709. [CrossRef]
8. Zapata, Y.; Kristensen, M.R.; Huerta, N.; Brown, C.; Kabir, C.S.; Reza, Z. CO_2 geological storage: Critical insights on plume dynamics and storage efficiency during long-term injection and post-injection periods. *J. Nat. Gas Sci. Eng.* **2020**, *83*, 103. [CrossRef]
9. Singh, A.K.; Boettcher, N.; Wang, W.; Park, C.H.; Goerke, U.J.; Kolditz, O. Nonisothermal effects on two-phase flow in porous medium: CO_2 disposal into a saline aquifer. *Energy Proc.* **2011**, *4*, 3889–3895. [CrossRef]
10. Benson, S.M.; Cole, D.R. CO_2 sequestration in deep sedimentary formations. *Elements* **2008**, *4*, 325–331. [CrossRef]
11. Agartan, E.; Trevisan, L.; Cihan, A.; Birkholzer, J.; Zhou, Q.; Tissa, H. Illangasekare. Experimental study on effects of geologic heterogeneity in enhancing dissolution trapping of supercritical CO_2. *Water Resour. Res.* **2015**, *51*, 1635–1648. [CrossRef]
12. Kumar, S.; Foroozesh, J.; Edlmann, K.; Rezk, M.G.; Lim, C.Y. A comprehensive review of value-added CO_2 sequestration in subsurface saline aquifers (Review). *J. Nat. Gas Sci. Eng.* **2020**, *81*, 103437. [CrossRef]
13. Zhang, D.; Song, J. Mechanisms for Geological Carbon Sequestration. *Procedia IUTAM* **2014**, *10*, 319–327. [CrossRef]
14. Saadatpoor, E.; Bryant, S.L.; Sepehrnoori, K. New trapping mechanism in carbon sequestration. *Transp. Porous Media* **2010**, *82*, 3–17. [CrossRef]
15. Burnside, N.M.; Naylor, M. Review and implications of relative permeability of CO_2/brine systems and residual trapping of CO_2. *Int. J. Greenh. Gas Control* **2014**, *23*, 1–11. [CrossRef]
16. Gershenzon, N.I.; Ritzi, R.W.; Dominic, D.F.; Mehnert, E.; Okwen, R.T. Comparison of CO_2 trapping in highly heterogeneous reservoirs with Brooks-Corey and van Genuchten type capillary pressure curves. *Adv. Water Resour.* **2016**, *96*, 225–236. [CrossRef]
17. Gershenzon, N.I.; Ritzi, R.W.; Dominic, D.F.; Mehnert, E.; Okwen, R.T. Capillary trapping of CO_2 in heterogeneous reservoirs during the injection period. *Int. J. Greenh. Gas Control* **2017**, *59*, 13–23. [CrossRef]
18. Adebayo, A.R. Sequential storage and in-situ tracking of gas in geological formations by a systematic and cyclic foam injection-A useful application for mitigating leakage risk during gas injection. *J. Nat. Gas Sci. Eng.* **2019**, *62*, 1–12. [CrossRef]
19. Xu, T.; Apps, J.A.; Pruess, K. Numerical simulation of CO_2 disposal by mineral trapping in deep aquifers. *Appl. Geochem.* **2004**, *19*, 917–936. [CrossRef]
20. Xu, T.; Apps, J.A.; Pruess, K. Mineral sequestration of carbon dioxide in a sandstone-shale system. *Chem. Geol.* **2005**, *217*, 295–318. [CrossRef]
21. Gaus, I.; Audigane, P.; Andre, L.; Lions, J.; Jacquemet, N.; Durst, P.; Azaroual, M. Geochemical and solute transport modelling for CO_2 storage, what to expect from it? *Int. J. Greenh. Gas Control* **2008**, *2*, 605–625. [CrossRef]
22. De Silva, G.P.D.; Ranjith, P.G.; Perera, M.S.A. Geochemical aspects of CO_2 sequestration in deep saline aquifers: A review. *Fuel* **2015**, *155*, 128–143. [CrossRef]
23. Gilmore, K.A.; Neufeld, J.A.; Bickle, M.J. CO_2 Dissolution Trapping Rates in Heterogeneous Porous Media. *Geophys. Res. Lett.* **2020**, *47*, e2020GL087001. [CrossRef]
24. Sathaye, K.J.; Hesse, M.A.; Cassidy, M.; Stockli, D.F. Constraints on the magnitude and rate of CO_2 dissolution at Bravo Dome natural gas field. *Proc. Natl. Acad. Sci. USA* **2014**, *111*, 15332–15337. [CrossRef] [PubMed]
25. Kim, K.Y.; Kim, M.; Oh, J. Core-scale investigation of the effect of heterogeneity on the dynamics of residual and dissolution trapping of carbon dioxide. *J. Hydrol.* **2021**, *596*, 126109. [CrossRef]
26. Sohal, M.A.; Le Gallo, Y.; Audigane, P.; de Dios, J.C.; Rigby, S.P. Effect of geological heterogeneities on reservoir storage capacity and migration of CO_2 plume in a deep saline fractured carbonate aquifer. *Int. J. Greenh. Gas Control* **2021**, *108*, 103306. [CrossRef]
27. Singh, M.; Chaudhuri, A.; Soltanian, M.R.; Stauffer, P.H. Coupled multiphase flow and transport simulation to model CO_2 dissolution and local capillary trapping in permeability and capillary heterogeneous reservoir. *Int. J. Greenh. Gas Control* **2021**, *108*, 103329. [CrossRef]
28. Onoja, M.U.; Williams, J.D.; Vosper, H.; Shariatipour, S.M. Effect of sedimentary heterogeneities in the sealing formation on predictive analysis of geological CO_2 storage. *Int. J. Greenh. Gas Control* **2019**, *82*, 229–243. [CrossRef]
29. Mouche, E.; Hayek, M.; Mugler, C. Upscaling of CO_2 vertical migration through a periodic layered porous medium: The capillary-free and capillary-dominant cases. *Adv. Water Resour.* **2010**, *33*, 1164–1175. [CrossRef]
30. Green, C.; Ennis-King, J.; Pruess, K. Effect of Vertical Heterogeneity on Long-Term Migration of CO_2 in Saline Formations. *Energy Procedia* **2009**, *1*, 1823–1830. [CrossRef]
31. Deng, H.L.; Stauffer, P.H.; Dai, Z.X.; Jiao, Z.S.; Surdam, R.C. Simulation of industrial-scale CO_2 storage: Multi-scale heterogeneity and its impacts on storage capacity, injectivity and leakage. *Int. J. Greenh. Gas Control* **2012**, *10*, 397–418. [CrossRef]
32. Kim, M.; Kim, K.-Y.; Han, W.S.; Oh, J.; Park, E. Density-driven convection in a fractured porous media: Implications for geological CO_2 storage. *Water Resour. Res.* **2019**, *55*, 5852–5870. [CrossRef]
33. Shafabakhsh, P.; Ataie-Ashtiani, B.; Simmons, C.T.; Younes, A.; Fahs, M. Convective-Reactive Transport of Dissolved CO_2 in Fractured-Geological Formations. *Int. J. Greenh. Gas Control* **2021**, *109*, 103365. [CrossRef]
34. Galkin, S.V.; Martyushev, D.A.; Osovetsky, B.M.; Kazymov, K.P.; Song, H. Evaluation of void space of complicated potentially oil-bearing carbonate formation using X-ray tomography and electron microscopy methods. *Energy Rep.* **2022**, *8*, 6245–6257. [CrossRef]

35. Martyushev, D.A.; Ponomareva, I.N.; Chukhlov, A.S.; Davoodi, S.; Osovetsky, B.M.; Kazymov, K.P.; Yang, Y. Study of void space structure and its influence on carbonate reservoir properties: X-ray microtomography, electron microscopy, and well testing. *Mar. Pet. Geol.* **2023**, *151*, 106192. [CrossRef]
36. Martyushev, D.A.; Govindarajan, S.K.; Li, Y.; Yang, Y. Experimental study of the influence of the content of calcite and dolomite in the rock on the efficiency of acid treatment. *J. Pet. Sci. Eng.* **2022**, *208*, 109770. [CrossRef]
37. Martyushev, D.A. Improving the geological and hydrodynamic model a carbonate oil object by taking into account the permeability anisotropy parameter. *J. Min. Inst.* **2020**, *243*, 313–318. [CrossRef]
38. Martyushev, D.A.; Ponomareva, I.N.; Osovetsky, B.M.; Kazymov, K.P.; Tomilina, E.M.; Lebedeva, A.S.; Chukhlov, A.S. Study of the structure and development of oil deposits in carbonate reservoirs using field data and X-ray microtomography. *Georesursy* **2022**, *24*, 114–124.
39. Oh, J.; Kim, K.Y.; Han, W.S.; Park, E.; Kim, J.C. Migration behavior of supercritical and liquid CO_2 in a stratified system: Experiments and numerical simulations. *Water Resour. Res.* **2015**, *51*, 7937–7958. [CrossRef]
40. Rasmusson, K.; Tsang, C.-F.; Tsang, Y.; Rasmusson, M.; Pan, L.; Fagerlund, F.; Bensabat, J.; Niemi, A. Distribution of injected CO_2 in a stratified saline reservoir accounting for coupled wellbore-reservoir flow. *Greenh. Gases Sci. Technol.* **2015**, *5*, 419–436. [CrossRef]
41. Lie, K.-A. *An Introduction to Reservoir Simulation Using MATLAB/GNU Octave: User Guide for the MATLAB Reservoir Simulation Toolbox (MRST)*; Cambridge University Press: Cambridge, UK, 2019.
42. Spycher, N.; Pruess, K. CO_2-H_2O mixtures in the geological sequestration of CO_2. II. Partitioning in chloride brines at 12-100 °C and up to 600 bar. *Geochim. Cosmochim. Acta* **2005**, *69*, 3309–3320. [CrossRef]
43. Spycher, N.; Pruess, K.; Ennis-King, J. CO_2-H_2O mixtures in the geological sequestration of CO_2. I. Assessment and calculation of mutual solubilities from 12 to 100 °C and up to 600 bar. *Geochim. Cosmochim. Acta* **2003**, *67*, 3015–3031. [CrossRef]
44. Wang, Y.; Fernàndez-Garcia, D.; Saaltink, M.W. Carbon Dioxide (CO_2) Dissolution Efficiency During Geological Carbon Sequestration (GCS) in Randomly Stratified Formations. *Water Resour. Res.* **2022**, *58*, e2022WR032325. [CrossRef]
45. Leverett, M.C. Capillary behavior in porous solids. *Trans. AIME* **1941**, *142*, 159–172. [CrossRef]
46. Buckley, S.E.; Leverett, M.C. Mechanism of fluid displacement in sands. *Trans. AIME* **1942**, *146*, 107–116. [CrossRef]
47. Juanes, R.; Spiteri, E.J.; Orr, F.M.; Blunt, M.J. Impact of relative permeability hysteresis on geological CO_2 storage. *Water Resour. Res.* **2006**, *42*, W12418. [CrossRef]
48. Krevor, S.C.; Pini, R.; Zuo, L.; Benson, S.M. Relative permeability and trapping of CO_2 and water in sandstone rocks at reservoir conditions. *Water Resour. Res.* **2012**, *48*, W02532. [CrossRef]
49. McWhorter, D.B.; Sunada, D.K. Exact integral solutions for two-phase flow. *Water Resour. Res.* **1990**, *26*, 399–413. [CrossRef]
50. Nordbotten, J.M.; Celia, M.A. Similarity solutions for fluid injection into confined aquifers. *J. Fluid Mech.* **2006**, *51*, 307–327. [CrossRef]
51. Bai, T.; Tahmasebi, P. Sequential Gaussian simulation for geosystems modeling: A machine learning approach. *Geosci. Front.* **2022**, *13*, 101258. [CrossRef]